

A hierarchical Bayesian approach to point source analysis in high-energy neutrino telescopes

FRANCESCA CAPEL ¹, JULIAN KUHLMANN ^{2,1}, CHRISTIAN HAACK ³, MARTIN HA MINH ²,
HANS NIEDERHAUSEN ⁴ AND LISA SCHUMACHER ³

¹*Max Planck Institute for Physics
Boltzmannstraße 8, 85748 Garching*

²*Technical University of Munich
James-Franck-Str. 1, 85748 Garching*

³*Erlangen Centre for Astroparticle Physics
Nikolaus-Fiebiger-Str. 2, 91058 Erlangen*

⁴*Michigan State University
288 Farm Lane, 48824 East Lansing MI*

Submitted to ApJ

ABSTRACT

We propose a novel approach to the detection of point-like sources of high-energy neutrinos. Motivated by evidence for emerging sources in existing data, we focus on the characterisation and interpretation of these sources. The hierarchical Bayesian model is implemented in the Stan platform, enabling computation of the posterior distribution with Hamiltonian Monte Carlo. We simulate a population of weak neutrino sources detected by the IceCube experiment and use the resulting data set to demonstrate and validate our framework. We show that even for the challenging case of sources at the threshold of detection and using limited prior information, it is possible to correctly infer the source properties. Additionally, we demonstrate how modelling flexible connections between similar sources can be used to recover the contribution of sources that would not be detectable individually, going beyond what is possible with existing stacking methods.

Keywords: High energy astrophysics (739) — Astronomical methods (1043) — Neutrino astronomy (1100) — Astrostatistics (1882) — Bayesian statistics (1900) — Hierarchical models (1925)

1. INTRODUCTION

Neutrino astronomy is in an exciting period, with the discovery of astrophysical neutrinos confirmed, but the search for their sources still ongoing (Kurahashi et al. 2022). Recent results from the IceCube Collaboration present evidence for the association of high-energy neutrinos with the blazar TXS 0506+056 (Aartsen

et al. 2018a,b), the Seyfert galaxy NGC 1068 (Abbasi et al. 2022a) and the Galactic plane (Abbasi et al. 2023). Independent analyses making use of public information also claim significant associations of neutrino events with blazars (Giommi & Padovani 2021; Buson et al. 2022, 2023), tidal disruption events (TDEs, Stein et al. 2021; van Velzen et al. 2021; Reusch et al. 2022), the Seyfert galaxies NGC 4151 and NGC 3079 (Neronov et al. 2024), and the Cygnus region (Neronov et al. 2023). However, few reports have crossed the 5σ significance threshold typically used to define detec-

tions and the physical interpretation of these results remains challenging.

The approach to searching for point sources in neutrino data used by the IceCube Collaboration makes use of hypothesis testing techniques in a likelihood-based frequentist framework, as described in [Braun et al. \(2008, 2010\)](#). The reconstructed event directions, energies, and angular uncertainties are used to distinguish source and background through a likelihood ratio test, comparing null and signal hypotheses. The significance of a potential source location is then calculated as a p -value by comparing the observed test statistic value in experimental data to the test statistic distribution expected under the null model.

We present an alternative approach to point source searches within the framework of Bayesian hierarchical modelling. The motivation is to make the most of existing data. Our framework can handle fits of complex models with large numbers of free parameters. As such, more information from both theory and experiment can be brought together resulting in more interpretable statistical analyses. With several large-scale neutrino observatories either in operation (IceCube: [Aartsen et al. 2017](#), Antares: [Ageron et al. 2011](#), Baikal-NT: [Belolaptikov et al. 1997](#)), in development (KM3Net: [Adrián-Martínez et al. 2016](#); Margiotta 2022; Baikal-GVD: [Avrorin et al. 2021](#); [Dvornicky 2023](#), P-ONE: [Agostini et al. 2020](#)) or planned in the future (IceCube-Gen2: [Aartsen et al. 2021](#), TRIDENT: [Ye et al. 2023](#)), we also focus on developing methods that can adapt and scale as we learn more about neutrino sources. As such, we focus on the characterisation of sources in addition to their discovery.

In this work, we introduce our method in Section 2 and demonstrate its performance on simulated data in Section 3. We then discuss the performance of our framework in the context of existing methods in Section 4 before concluding in Section 5. The code used in this work and relevant examples are available in the `hierarchical_nu`¹ python package.

2. METHODS

Our approach is centred on the derivation of a hierarchical or multi-level likelihood function that captures the key phenomenology of astrophysical neutrino production and detection. We start with the high-level model parameters and connect to the observables: the neutrino energies and arrival directions, along with their respective reconstruction uncertainties. We describe the key aspects of the physical model and the statistical implementation here.

2.1. Physical model

We consider point-like sources of astrophysical neutrinos with a power-law spectrum defined between source frame energies E'_{\min} and E'_{\max}

$$\frac{d^2n}{dE dt} \propto E^{-\gamma_s}, \quad (1)$$

where γ_s is the spectral index. The isotropic source luminosity with this energy range leads to an energy flux at Earth

$$F = \frac{L}{4\pi D_L^2(z)} \quad (2)$$

in the redshifted energy range $E_{\min, \max} = E'_{\min, \max}/(1+z)$, where $D_L(z)$ is the luminosity distance at redshift z . It then follows that the differential flux from a single source at Earth is given by

$$\frac{d^3n}{dE dt dA} = \frac{Lk_\gamma E^{-\gamma_s}}{4\pi D_L(z)^2} = \phi_s \left(\frac{E}{E_0} \right)^{-\gamma_s}, \quad (3)$$

where k_γ is defined such that the spectrum is normalised to L in the source frame and in the final step we introduce the normalisation energy, E_0 , and summarise the differential flux at E_0 as ϕ_s . Throughout this work, we assume a flat Λ CDM cosmology with $H_0 = 70 \text{ km s}^{-1} \text{ Mpc}^{-1}$, $\Omega_m = 0.3$ and $\Omega_\Lambda = 0.7$. We choose a standard power-law spectral model for point sources here to allow for straightforward comparison to other methods. However, more complex modelling possibilities are implemented in our framework and we plan to explore their application in future work.

In addition to point sources, we also consider two diffuse components as possible sources of neutrino emission: a diffuse astrophysical background and an atmospheric background.

Individual sources of interest typically belong to a population of objects with similar astrophysical properties. In point-source searches,

¹ https://github.com/cescalara/hierarchical_nu (to be made available upon publication)

we typically only hope to resolve some fraction of the total population of sources. Additionally, individual sources or lists of sources may not be solely responsible for the observed astrophysical flux. With these factors in mind, we model a diffuse astrophysical component that accounts for any astrophysical flux that cannot be associated with resolved point sources. To avoid assumptions on the cosmological distribution or luminosities of these unknown sources, we simply model this contribution as an isotropic spectrum over the whole sky described as

$$\frac{d^4n}{dE dt dA d\omega} = \phi_d \left(\frac{E}{E_0} \right)^{-\gamma_d}, \quad (4)$$

where ϕ_d is the differential flux normalisation at E_0 , and γ_d is the spectral index of the bounded power law spectrum that is defined between E_{\min} and E_{\max} . This spectral model is standard in diffuse astrophysical neutrino analyses, but could be adapted as new information becomes available (see e.g. Naab et al. 2023).

Another important diffuse background, particularly at energies $E < 100$ TeV, is that due to atmospheric neutrinos, produced by the interactions of cosmic rays in our Earth's atmosphere. The atmospheric neutrino flux depends on the zenith angle and the spectrum is not well-described by a single power law. Therefore, we use MCEq (Fedynitch et al. 2015) to model the atmospheric arrival direction distribution and spectra. We use the H4a cosmic ray flux model described in Gaisser (2012), the atmospheric density profile implemented in NRLMSISE-00 (Picone et al. 2002) and SIBYLL 2.3c to model hadronic interactions (Riehn et al. 2017). Furthermore, we assume that the normalisation of the atmospheric flux is not exactly known and parameterise it as Φ_a .

High-energy neutrino telescopes measure the secondary Cherenkov radiation produced when incoming neutrinos interact in a large instrumented volume of water or ice. The energies and arrival directions of the primary neutrinos are not observable, but the reconstructed energies and directions of secondaries serve as a proxy. The reconstruction of these observables yields an associated uncertainty. Here, we consider the IceCube neutrino observatory to demonstrate our approach, but it is straightforward to extend our framework to other exper-

iments. In particular, we consider the publicly available data of track-like events from muon neutrino interactions (IceCube Collaboration 2021) that is used in Aartsen et al. (2020a), but with limited information on the provided instrument response functions (IRFs). The IRFs consist of the effective area, A_{eff} , as function of neutrino energy, E , and declination, δ . Further, the energy resolution and point spread function are available as a tabulated mapping from E and δ to \hat{E} and $\hat{\omega}$. The corresponding public data set lists reconstructed muon events with energy \hat{E} , and direction $\hat{\omega}$. Further details are discussed in Appendix A.

2.2. Statistical formalism

The aim of our statistical framework is to quantify the association of neutrinos with possible sources, whilst simultaneously inferring the physical properties of these sources. We expect sources to share similar characteristics across their classes or populations, making a hierarchical framework a natural approach.

Our method builds on a hierarchical mixture model formalism for cross-identification (see e.g. Budavári & Loredo 2015), extended to account for reconstructed event energies as well as directions, important selection effects in the observed samples, and relevant source properties (Capel & Mortlock 2019). The likelihood has the form of an inhomogeneous Poisson point process, the rate of which is a mixture model over the different possible source contributions. This can be written as (Streit 2010)

$$\mathcal{L}(E, \Theta) = e^{-\bar{n}_\nu^{\text{tot}}} \prod_{i=1}^{n_\nu} \sum_{j=1}^{N_c} r_j(\hat{E}_i, \hat{\omega}_i | E_i, \Theta_j), \quad (5)$$

for n_ν detected neutrino events and N_c model components (where $N_c = N_s + 2$ diffuse components). The expected number of detected neutrino events, \bar{n}_ν^{tot} , is given by the sum over all model components such that $\bar{n}_\nu^{\text{tot}} = \sum_{j=0}^{N_c} \bar{n}_j$. Similarly, the expected number of events from point sources is given by $\bar{n}_\nu = \sum_{j=0}^{N_s} \bar{n}_j$. We summarise the vector of all high-level parameters as Θ , and the subset of those relevant for individual model components as Θ_j . All energies are summarised as E . For N_s point sources, $\Theta_j = \{L_j, \gamma_j, \omega_j, D_j\}$, whereas for the diffuse astrophysical and atmospheric components $\Theta_j = \{\Phi_d, \gamma_d\}$ and

$\Theta_j = \{\Phi_a\}$, respectively. r_j is the j -th component’s rate parameter, relating to the number of expected events, \bar{n}_ν^{tot} , through integration as shown in Eq. (A1). The relationship between parameters in Eq. (5) is summarised graphically in Fig. 1 for the case of point source components.

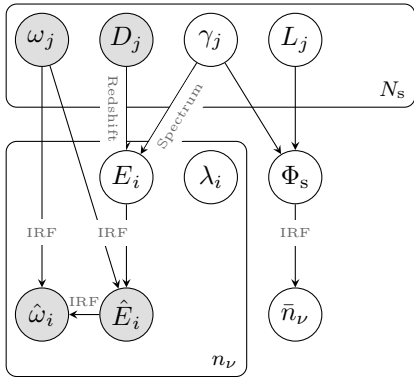


Figure 1. Summary of the likelihood for point source components. Open and shaded circles are used to show model parameters and fixed observables respectively, with the arrows showing the connections between them. The boxes are used to separate the N_s source components and n_ν events. The parameters are explained in the text. The levels from upper to lower show the source properties, latent true parameters and quantities that depend on the IRF. The latent source labels, λ_i , are discrete parameters marking the mixture model component that each event belongs to.

All model parameters are left free, but the highest-level parameters also have associated prior distributions. As a default, we make use of weakly informative priors for these parameters, as shown in Table 1. Such priors allow us to include our knowledge on reasonable physical values, while not driving the results of the eventual inference. In Section 3.3, we also demonstrate the application of more informative priors, as could be motivated by, e.g., multi-messenger information or theoretical predictions. Where relevant, we verify that the results are robust to reasonable variations in the choice of priors.

For a given data set of n_ν neutrino events, we perform inference on the model parameters in a Bayesian framework. The posterior distribution is proportional to the likelihood given in Eq. (5) multiplied by the joint prior summarised in Table 1. We generate samples from this posterior using *Stan* (Stan Develop-

	Distribution	Units
L/L_j	Lognorm(8.0×10^{43} , 4.0)	erg s^{-1}
γ_s/γ_j	Norm(2.0, 0.25)	–
Φ_d	Lognorm(5.4×10^{-8} , 0.3)	$\text{cm}^{-2} \text{s}^{-1}$
γ_d	Norm(2.5, 0.04)	–
Φ_a	Lognorm(3.0×10^{-5} , 0.08)	$\text{cm}^{-2} \text{s}^{-1}$

Table 1. Default prior assumptions for model hyperparameters, given as the distributions used and the corresponding μ and σ values. L/L_j is bounded between $[0, 10^{52}] \text{ erg s}^{-1}$, Φ_d and Φ_a are also bounded between $[10^{-10}, 10^{-7}]$ and $[0, 3 \times 10^{-4}] \text{ cm}^{-2} \text{ s}^{-1}$. Both γ_s/γ_j and γ_d are bounded between 1 and 4.

ment Team 2024), which implements an efficient variant of a Markov chain Monte Carlo algorithm called Hamiltonian Monte Carlo. This class of algorithm guarantees convergence to the target distribution in the limit of infinite samples. Here, we use a set of diagnostics to assess convergence in the case of finite samples. In particular, we run 4 separate chains of 2000 samples each (1000 warm-up samples to tune the algorithm and find the target distribution, 1000 actual samples of the target distribution) and require an effective sample size, $n_{\text{eff}} > 1000$ and a Gelman-Rubin statistic, $\hat{R} < 1.1$ with no divergent transitions for all model parameters in our analyses (Gelman et al. 2013).

2.3. Interpretation of results

The results of the fits using *Stan* take the form of samples representing the joint posterior distribution over all model parameters, also including latent parameters. Useful summaries of the fit parameters can be derived from these samples, such as the most probable value and highest posterior density interval (HDI), representing the “best-fit” value and its associated uncertainty. We evaluate the “goodness-of-fit” using posterior predictive checks (PPCs), which involve generating simulated data under the assumptions of the fitted model and comparing to the observed data to check the inferences are reasonable (Gelman et al. 2013, Chapter 6.3).

As shown in Fig. 1, each neutrino event has a latent true energy parameter, E_i . The marginal posterior of this parameter provides additional information useful to the interpretation of the origin of this event, considering

all possible model components and uncertainties, which is non-trivial to infer from the reconstructed event energies, \hat{E}_i , alone.

To directly address the possible association of neutrino events with source components of the model, we introduce additional derived parameters that capture the relevant information. Each neutrino event has a discrete label parameter, λ_i , which identifies its source component. While the λ_i are not explicitly sampled during inference, we can compute the marginal posterior distribution for λ_i , $\Pr(\lambda_i = j | \hat{E}, \hat{\omega})$, as shown in Appendix B. This marginal posterior gives the association probability for each event–source component pair given the available data, allowing for a more direct and insightful interpretation of the results.

We can also quantify discovery and sensitivity within this Bayesian framework. For individual event–source associations, we can confidently claim an association if

$$\Pr(\lambda_i = j | \hat{E}, \hat{\omega}) > \alpha, \quad (6)$$

where α is a threshold probability to be defined. However, the information in individual events is naturally limited, and therefore if using small event sample sizes it is important to study the prior dependence of the association probability (see Capel et al. 2023 for an example). A useful parameter that summarises our expectation over the whole sample of possible event–source associations is the expected number of detected neutrinos from the j -th point source, \bar{n}_j . We define the detection of a source as

$$\Pr(\bar{n}_j \geq 1 | \hat{E}, \hat{\omega}) > \alpha. \quad (7)$$

In the case of a non-detection or when quantifying the sensitivity, we can find the HDI of Φ_j or L_j for a given probability level, α , and report the corresponding upper limit.

The probability thresholds, α , defined above are somewhat arbitrary and are not directly comparable to a p -value from a frequentist analysis. It is possible to calibrate α via repeated simulations to give some desired coverage, true detection rate or false detection rate (Betancourt 2018). However, within a Bayesian framework, the resulting posterior probability for event–source associations or expected number of events is itself the main result. For the purpose of this work we choose $\alpha = 0.95$ (similar definitions can be found in,

e.g., Aggarwal et al. 2021; Sottosanti et al. 2021). This is not equivalent to a p -value of 0.05, and is importantly a statement about the alternate hypothesis (point-source model components) rather than the null hypothesis (diffuse background model components).

3. APPLICATION

In this work, we focus the application of our method to a population of weak sources that are below the detection threshold of existing methods.

3.1. Simulated data set

We simulate a population of neutrino sources using `popsynth` (Burgess & Capel 2021), characterised by the physical properties introduced in Section 2.1: a redshift, z , a luminosity, L , a spectral index, γ , and a direction, ω . We choose a source redshift evolution based on the shape of the star formation rate given in Madau & Dickinson (2014) and a luminosity function that is described by a broken power law. Source spectral indices follow a Gaussian distribution and sources are distributed isotropically on the sky. The choices regarding the source population properties are detailed in Table 2.

	Distribution
z	$\frac{dN}{dV} = 100 \frac{1+4.8z}{1+(z/2.7)^{3.9}} \text{ Gpc}^{-3} \text{ sr}$
L	$\frac{dN}{dL} = \begin{cases} CL^{-2} & \text{if } L \leq L_{\text{br}} \\ CL^{-3} L_{\text{br}} & \text{if } L > L_{\text{br}} \end{cases} \text{ erg}^{-1} \text{ s}$
γ	$\frac{dN}{d\gamma} = \text{Norm}(2.0, 0.25)$
ω	$\frac{dN}{d\omega} = \frac{1}{4\pi} \text{ sr}^{-1}$

Table 2. Source population properties and their distributions. We use $L_{\text{br}} = 5 \times 10^{44} \text{ erg s}^{-1}$ and C is defined such that the distribution is normalised to 1. The the following ranges are also used: $z \in [0, 6]$, $L \in [5 \times 10^{43}, 5 \times 10^{48}] \text{ erg s}^{-1}$ and $\gamma \in [1, 4]$.

Our source population is set up to provide a generic but relevant test scenario that is not connected to a particular class of astrophysical sources. We ensure that our simulated population is consistent with general population constraints (Murase & Waxman 2016; Capel et al. 2020) in that it does not exceed the measured diffuse astrophysical neutrino flux and sources are neither too rare nor too bright. Beyond $z \sim 0.5$, the neutrino signal from the popula-

tion is effectively diffuse ($\bar{n}_\nu \lesssim 1$ for individual sources).

To generate our simulated neutrino data set, we select sources in the Northern hemisphere ($\delta > -5^\circ$) with $F \geq 5 \times 10^{12}$ erg cm $^{-2}$ s $^{-1}$, giving $N_s = 6$. The properties of these selected sources are given in Table 3.

Fig. 2 shows the selected sources in comparison with the sensitivity and discovery potential of `skyllh`, which implements a frequentist approach that is typically used in neutrino point source searches (Wolf 2019; Bellenghi et al. 2023a). The sensitivity flux is calculated as the median 90% CL upper limit on the flux normalisation over repeated simulations of only background. The discovery potential is defined as the flux that leads to a 5σ deviation from the background expectation in 50% of repeated simulations. The same curves from Aartsen et al. (2020b) are also shown, but as these have been calculated using more detailed detector Monte Carlo that is not publicly available, they do not represent a fair comparison in this work.

All sources are below the estimated discovery potential, but it is important to note that the sensitivity and discovery potential fluxes are calculated for a fixed power-law spectrum with index $\gamma_s = 2$, while the point sources simulated here have γ_j in the range [1.62, 2.52]. In Fig. 2, we also show the corresponding number of events in our simulation. This visualisation better accounts for the different spectral index assumptions, but the number of events required for a detection in a given simulation will depend on their energies. In this work, we only investigate one possible realisation of our simulation and Fig. 2 is only intended to provide a rough comparison with existing work.

All other sources from the population are treated as a sub-dominant contribution to the diffuse flux and are not simulated explicitly. We include a diffuse astrophysical flux with $\phi_d = 1.8 \times 10^{-18}$ GeV $^{-1}$ cm $^{-2}$ s $^{-1}$ sr $^{-1}$ and $\gamma_d = 2.5$ based on recently reported observations (Abbasi et al. 2022b; Naab et al. 2023; Abbasi et al. 2024). The atmospheric flux is also included using MCEq as described in Section 2.1. All source components are simulated over a wide energy range from $E_{\min} = 100$ GeV to $E_{\max} = 100$ PeV. We simulate the detection of neutrinos from these source components using the provided IRF and place a cut on the reconstructed muon energy of $\hat{E}_{\min} = 300$ GeV.

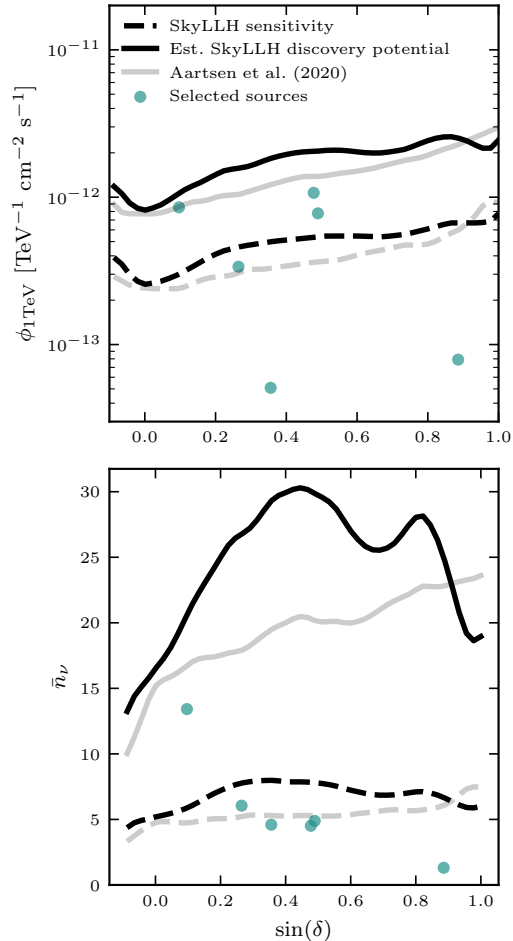


Figure 2. **Upper panel:** The differential flux normalisation at 1 TeV for simulated point sources. The SkyLLH sensitivity assuming an E^{-2} power-law spectrum as reported in Bellenghi et al. (2023a) is shown for comparison, as this calculation makes use of the same publicly available IRF that is used here. We also plot an estimation of the discovery potential by rescaling the sensitivity as a function of declination. This rescaling is calculated as the ratio of the discovery potential to the sensitivity, according to the results presented in Aartsen et al. (2020b), which are also shown for comparison. **Lower panel:** The total expected number of neutrino events for simulated point sources is shown in comparison to that required by the sensitivity and discovery potential curves introduced above.

This choice is to include thresholding effects due to events with true energies $E < 300$ GeV being mis-reconstructed above \hat{E}_{\min} and vice versa. For this simulated data set, we simulate n_j as the most likely integer value based on \bar{n}_j , for a clearer interpretation and discussion of the different source cases in the next

	$(RA, \delta)_j$	z	L_j	$\gamma_s j$	n_j	
	[$^\circ$]		[erg s^{-1}]		$\geq 300 \text{ GeV}$	$\geq 1 \text{ TeV}$
1	(183.6, 5.5)	0.04	5.8×10^{43}	2.05	14	11
2	(56.0, 29.3)	0.43	5.8×10^{45}	2.30	7	6
3	(273.2, 28.5)	0.13	5.3×10^{44}	2.52	5	5
4	(23.8, 15.4)	0.06	6.6×10^{43}	1.99	4	4
5	(179.6, 20.8)	0.17	1.6×10^{45}	1.62	2	2
6	(325.0, 62.3)	0.12	1.81×10^{44}	1.81	1	1

Table 3. Properties of the simulated neutrino point sources. Sources are listed in order of decreasing number of simulated events, n_j , that are included in the event selection used here.

sections. A summary of the resulting data set is shown in Fig. 3.

3.2. Single source analysis

To demonstrate the analysis of individual sources in our framework we focus on the point source that has the most detected events in our simulated data set, source #1 from Table 3. We make a selection on our data set, defining a circular region of interest (ROI) on the sky centred on the source location with a radius of 5° .

We use our method to fit the data in this ROI, using the priors detailed in Table 1. We show the results for the marginal posterior of the source parameters in Fig. 4, demonstrating the correct reconstruction of the known true parameter values.

The marginal posterior of the expected number of neutrino events from source #1, \bar{n}_1 , is given in Fig. 5. To validate the correct reconstruction of \bar{n}_1 , we also fit data sets where we add in source events one by one. Fig. 5 also shows the resulting \bar{n}_1 posterior for $n_\nu = [0, 5, 10, 14]$. We can see that in the case of $n_\nu = 0$, the \bar{n}_1 posterior is strongly peaked at zero and gradually moves away in a consistent manner as more point source events are added to the simulation. Using the definition of source detection given in Eq. (7) with $\alpha = 0.95$, we can identify this source above the detection threshold in the simulated dataset that includes all 14 source events. We also performed fits to 100 simulations of background-only events, verifying that none of these re-

sult in false point-source detections according to our detection criterion.

Our framework further enables us to give posterior association probabilities of single events to each source component, as detailed in Section 2.3. We summarise this information in Fig. 6 in terms of both the event positions and energies. We see that the higher energy events that are closer to the source have a larger association probability, as expected. Point source events that have a low association probability are mostly mis-reconstructed as belonging to the atmospheric background component, which dominates at lower energies. Using the event-based definition of association given in Eq. (6), only the event with the second highest \hat{E} value passes the threshold with an association probability of 0.99. The event with the highest \hat{E} value is close behind, with an association probability of 0.95.

In Fig. 6, we see the complementary information that is available in terms of the individual event–source association probabilities. For example, Fig. 5 shows that the overall \bar{n}_1 posterior is consistent with 14 events for source #1, but Fig. 6 shows that we have probable individual associations for only about half of these events, typically at higher energies. The remaining contribution to \bar{n}_1 comes from many events with smaller association probabilities. We can also see that for events that have a $\sim 50\%$ association probability, the posterior for E can have two peaks, corresponding to the possible latent E that would best fit the source or background components.

As means of verifying goodness-of-fit we perform PPCs. Histograms of \hat{E} and $\hat{\omega}$ for 100 generated data sets from the posterior predictive distribution are shown in Fig. 7, indicating no obvious signs of mismodelling from visual

² We verified that for the source modelling assumptions used here and the angular resolution provided by the IRF, this radius is large enough to avoid impacting the results.

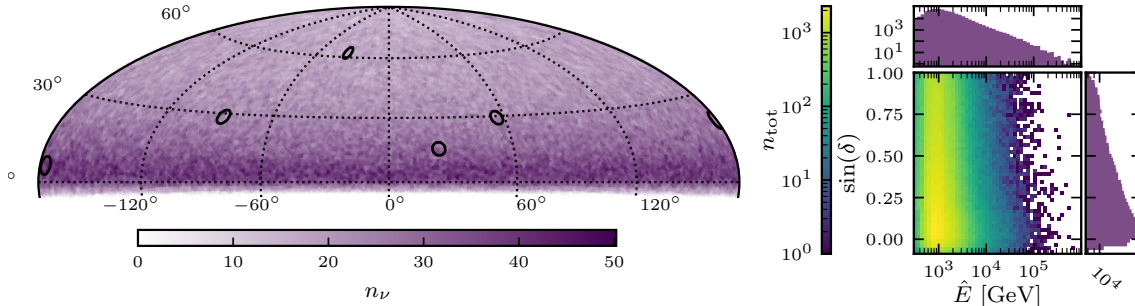


Figure 3. The simulated data set. The left panel shows a skymap of the event directions with the selected source positions overlaid. The right panel shows the distribution of events in \hat{E} and $\sin(\delta)$, cf. Fig. 1 in [IceCube Collaboration \(2021\)](#).

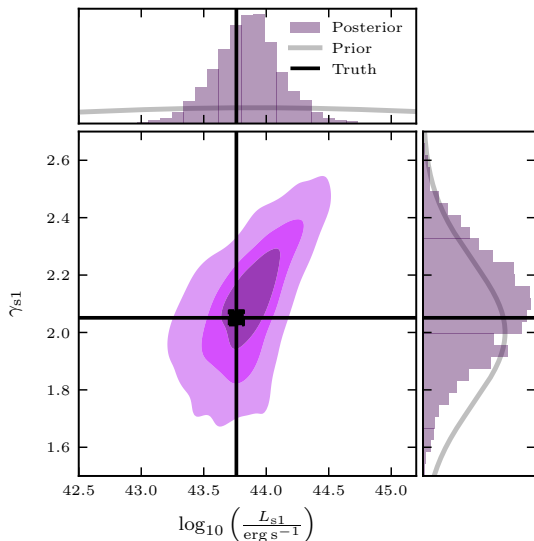


Figure 4. The joint posterior density of L and γ_s with contours showing the 30%, 60% and 90% HDIs. The true parameter values are indicated by the horizontal and vertical solid lines. The upper and right panels show the marginal distributions in comparison with the prior.

inspection. We also quantified the discrepancy in each bin by calculating a p -value, and found only relatively large p -values that followed a uniform distribution between 0 and 1.

3.3. Joint analysis of multiple sources

We now perform joint fits of all six selected point sources. Motivated by computational considerations, we make a further cut of $\hat{E} \geq 1$ TeV on our simulated dataset, as only 4 of the total 33 point source events are lost in this case (see Table 3). Additionally, based on the results in Section 3.2, we do not expect the lower energy events to contribute to the detectability of these sources. Our framework is designed to allow for flexible definitions of possible connections between individual sources,

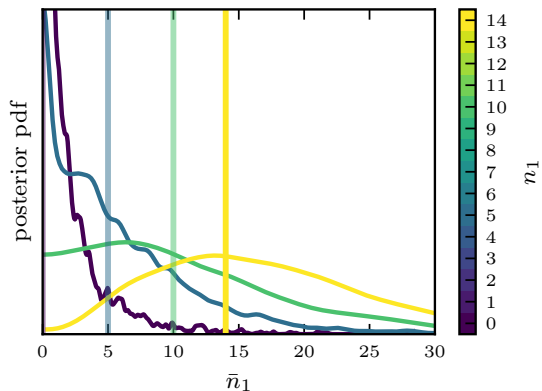


Figure 5. Marginal posterior density of the expected number of point source events for source #1, \bar{n}_1 . The number of selected source events in each fit is colour coded, with $n_1 = [0, 5, 10, 14]$ shown.

and we explore three cases here as examples: 1) All sources share the same luminosity, L , and spectral index, γ_s ; 2) All sources have individual and unknown L_j and γ_j ; and 3) Informative priors on the individual L_j and γ_j . We note that our framework can also handle the case between 1) and 2), including some balance between global and individual source parameters, and this is discussed further in Section 4.

For the joint fits, all information shown in Section 3.2 is available and can be analysed independently for all sources. The difference between fitting all sources separately is that the joint fit allows the results of one source to influence the others, according to the details of the model for their population. For brevity, we focus here on few key results that highlight the implications of the three example cases introduced above. Fig. 8 shows the marginal posterior distributions for the point source luminosity, L and the expected number of events from

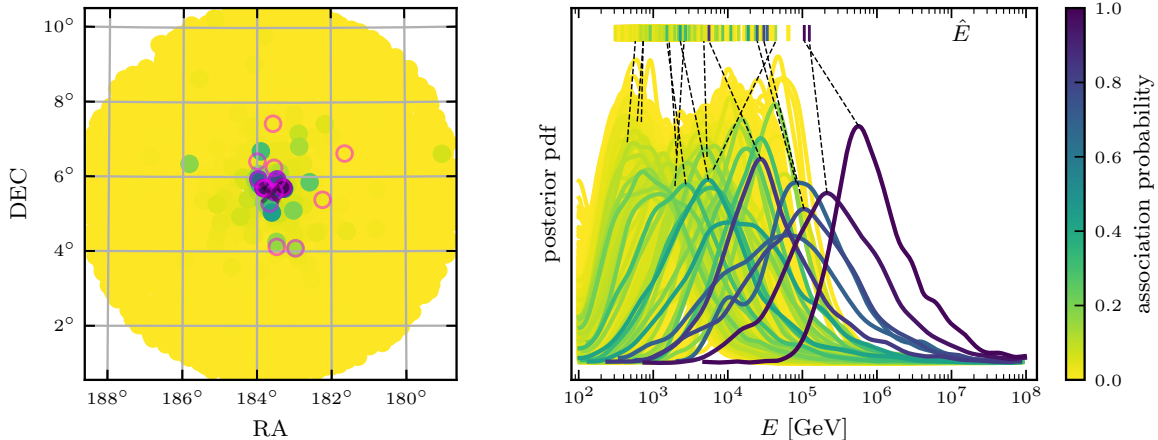


Figure 6. Colour-coded posterior association probabilities of events to source #1. **Left panel:** Spatial distribution of events. The marker size does not represent the angular resolution and the point source events are highlighted in red borders. **Right panel:** Marginal posteriors for the true neutrino energies of events included in the ROI. Markers on the top row indicate \hat{E} for all events included in the analysis, with dashed connecting lines to the posteriors for the events from the tested point source.

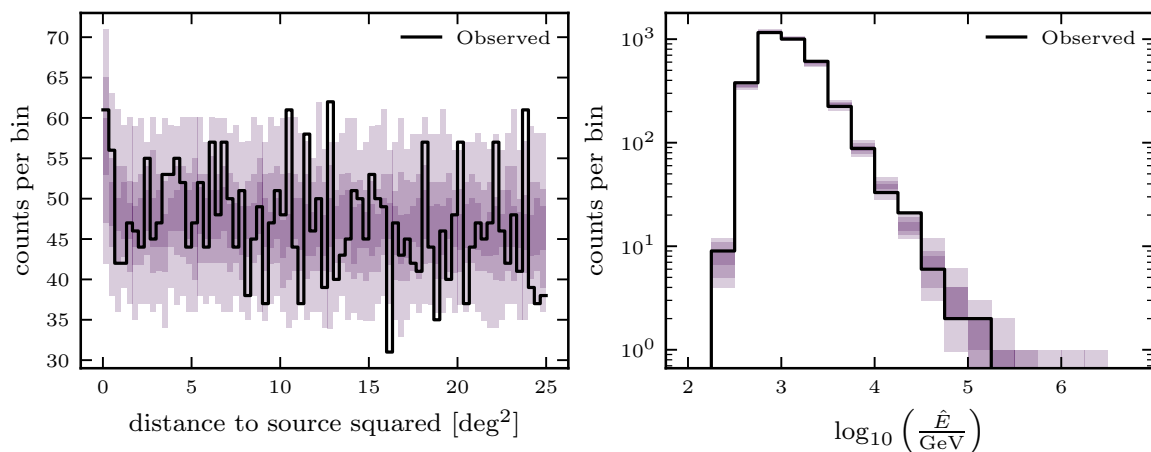


Figure 7. Distribution of observed and posterior predictive data. Shaded bands show 30%, 60%, and 90% quantiles from darkest to lightest.

each source, \bar{n}_ν , for each of the three studied cases.

For the first case of shared L and γ_s , we see that the source with most events, source #1, drives the values of these parameters. As this source has a relatively low L^3 , \bar{n}_j is reduced for all sources other than source #4, which has a similar L . For this case, γ_s is relatively unconstrained due to the low event numbers, so there is only a slight information gain of the posterior relative to the prior. The overall impact is the underestimation of \bar{n}_j for harder sources, such as sources #3, #5 and #6.

³ Despite having a low L , as source #1 is the closest source, it still has the highest number of detected events in the simulated data set.

For the case of individual free source parameters, L_j and γ_j , the variety of the sources is better captured. While the L_j and n_j posteriors are all consistent with the corresponding true values, the distributions remain relatively unconstrained for sources #2, #4 and #6. The γ_j posteriors show some shift away from the prior for sources #5 and #1, but are otherwise rather similar to the posterior from the shared parameter case above.

Finally, we investigate using informative priors for the individual L_j and γ_j . Cases 1) and 2) both use shared priors for the source parameters, as described in Table 1. We now suppose that further information is available on the L_j and γ_j for the individual sources. This could be in the form of, e.g., neutrino observations of

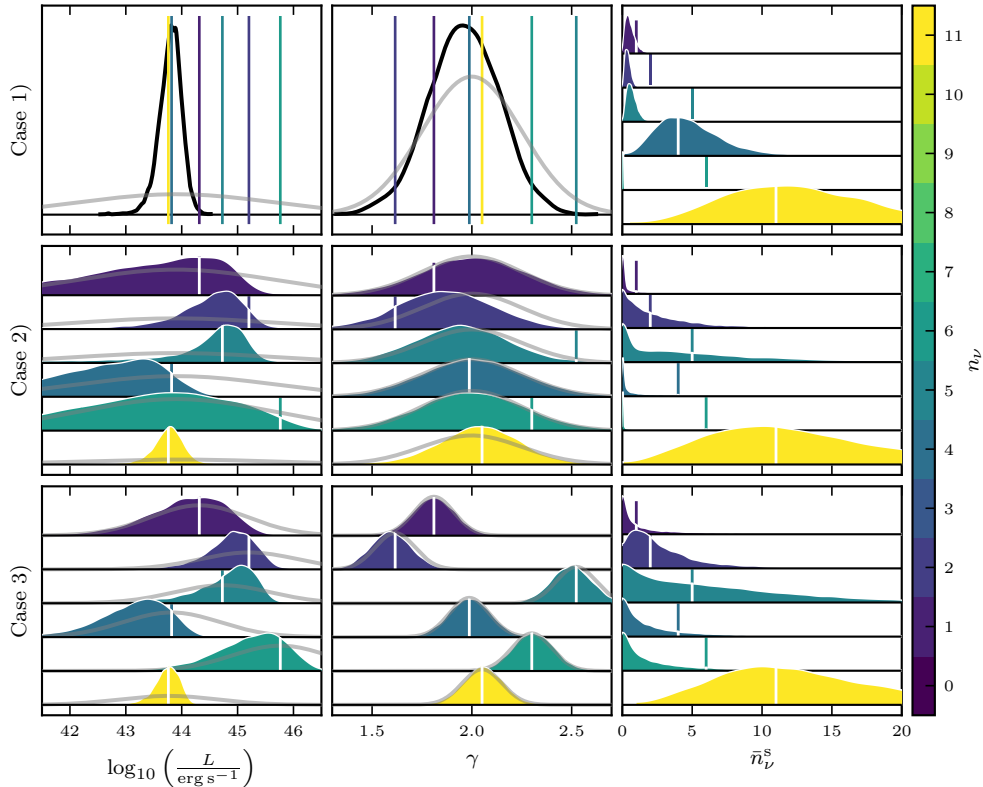


Figure 8. The marginal posteriors for L , γ_s and \bar{n}_j for all 6 point sources, shown by the different colours. The upper, middle and lower rows show the results for cases 1), 2) and 3), respectively. The true values are indicated as solid vertical lines and the priors are shown in grey, where relevant.

other sources, multi-messenger information, or theoretical predictions. We use log-normal priors for L_j , centred on the true values and with a width of 2.0. For the γ_j , we use normal priors centred on the true values with $\sigma_\gamma = 0.1$. While informative, these priors still allow for the possibility that $\bar{n}_j = 0$ for all sources, and the allowed parameter ranges leave room for the data to drive the posterior results. We see that in this case, we have better reconstruction of both L_j and \bar{n}_j for all sources, but the most impact is seen for sources #2, #4, and #6, which were the least constrained in case 2). The γ_j posteriors mostly follow the priors, with no strong additional constraints from the data.

We further summarise the above results for the three example cases by comparing the results for the total number of expected point source events across all sources, \bar{n}_ν , as shown in Fig. 9. We see that assuming the L and

γ_s are shared by all sources as in case 1), we underestimate the total contribution of these point sources as $\sim 1/2$ of the true value. For case 2) we improve the result, but still underestimate the contribution as only $\sim 3/4$ of the truth and the extra information in case 3) is necessary to recover the contribution from all point sources. As $\Pr(\bar{n}_\nu \geq 1 | \hat{E}, \hat{\omega}) = 1.0$ for all cases, it makes more sense to state the \bar{n}_ν threshold for which this expression is > 0.95 . For cases 1), 2) and 3) this is 7, 9 and 14, respectively. We can interpret this as a confident detection of this many events from all point sources included in the fit.

We give the $\Pr(\bar{n}_j \geq 1 | \hat{E}, \hat{\omega})$ values for each source considered in Table 4. Interestingly, for case 1), both sources #1 and #4 are detectable according to the definition in Eq. (7) with $\alpha = 0.95$, but only source #1 remains detectable for cases 2) and 3). This can be understood as sources #1 and #4 have very

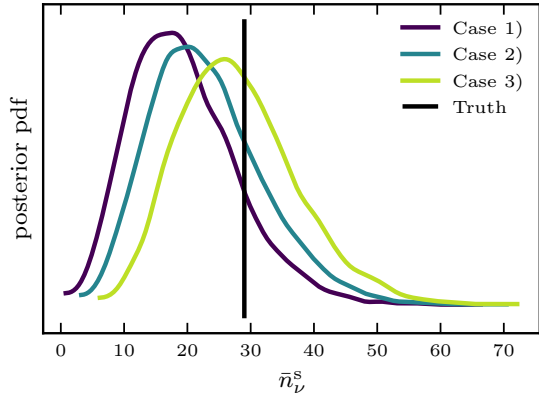


Figure 9. The marginal posterior distributions for \bar{n}_ν from all 6 point sources for the three example cases discussed in Section 3.3.

similar L_j and γ_j , so it is beneficial to assume shared parameters in this case, especially given the strength of source #1. However, the overall detectability of all sources is better served by considering their individual properties, and the value of $\Pr(\bar{n}_j \geq 1 | \hat{E}, \hat{\omega})$ increases significantly for all sources other than #4.

Source	$\Pr(\bar{n}_j \geq 1 \hat{E}, \hat{\omega})$		
	Case 1	Case 2	Case 3
#1	0.998	0.998	1.000
#2	0.000	0.098	0.566
#3	0.158	0.777	0.859
#4	0.989	0.305	0.568
#5	0.007	0.661	0.769
#6	0.110	0.316	0.436

Table 4. Impact of the three different modelling assumptions described in the text on the detectability of all sources considered.

The event–source association probabilities generally reflect the results discussed above. It is worth mentioning that source #5 produces an event with $\hat{E} = 1.3$ PeV in our simulation, which has an association probability of 0.92, 0.95 and 0.99 for cases 1), 2) and 3), respectively. As this is a faint source with only 2 simulated events and more extreme properties, it makes sense that the association probability increases as we allow the sources to have independent parameters and include more prior information.

4. DISCUSSION

The results shown in Section 3.2 and 3.3 demonstrate the validity of our method and introduce the possible analyses that can be performed within this framework. In addition to parameter estimation, we address how probabilities of interest can be quantified, such as the event–source association probability and the probability that a source or population contributes at least \bar{n}_ν events to the data. The most relevant output will typically depend on the details of the application to different physical scenarios. For example, the event–source association probabilities are likely most useful for studying high-energy neutrino alert events or analysing the impact of different source spectral models on possible associations. On the other hand, the overall expected event contribution is a direct way to investigate the detectability of sources and their populations that naturally includes the relevant uncertainties. Example applications could include characterising a population of hard-spectrum sources that TXS 0506+056-like sources to (Buson et al. 2022, 2023; Bellenghi et al. 2023b), or constraining the contribution from a population of NGC 1068-like sources (Glauch et al. 2023; Saurenhaus & Capel 2023). With our framework, we aim to provide a consistent setting for application to these different cases.

In Section 3.3, we also illustrate the power that including more information into the analysis can have when trying to detect a number of weak sources in the data. Even for events with a relatively poor energy resolution, we see in Fig. 9 that including prior information on the spectral index makes a significant difference when estimating the contribution of these point sources. For a non-detection, this equates to stronger constraints on the proposed model, allowing us to make the most of the available data in either case.

Several recent works in the field of multi-messenger astrophysics explore Bayesian approaches for individual source–event associations (see e.g. Ashton et al. 2018, Bartos et al. 2019 and Veske et al. 2021, Kowalski 2021). These methods still frame the problem as a hypothesis test, preferring Bayes factors and odds ratios to p -values, or using the Bayes factor as a test statistic in order to draw conclusions. Here, we focus more on addressing the questions of interest via parameter estimation

rather than model comparison. The foreseen workflow is to be able to develop and refine models that are consistent with the data, while exploring their implications. In this workflow, model rejection is a subset of the possible outcomes.

Frequentist hypothesis testing methods are typically used in searches for neutrino point sources. In particular, likelihood ratio methods as introduced in [Braun et al. \(2008\)](#) and implemented in [SkyLLH \(Wolf 2019; Bellenghi et al. 2023a\)](#) have been used in IceCube analyses to find evidence for TXS 0506+056, NGC 1068 and the Galactic plane as neutrino sources ([Aartsen et al. 2018a,b; Abbasi et al. 2022a, 2023](#)). We see our Bayesian approach as complementary to the standard methods in that the focus is on the evaluation and characterisation of source models rather than the rejection of the background-only hypothesis. Due to the different definition of probability in frequentist and Bayesian statistics and the different goals of these two methods, it is non-trivial to directly compare their performance. As such, we only make qualitative comparisons in this work and highlight the complementary features below.

With our definition of detection and the realisation of the simulated dataset studied, we can detect source #1 with only weakly informative priors, as well as source #4 when assuming shared source parameters as in case 1) of [Section 3.3](#). Source #5 has one very high energy event and is therefore detectable for case 3). Sources #2, #3 and #6 cannot be detected independently as they are softer (#2 and #3) or happen to only produce lower energy events in this simulated data set (#6), but their contribution to the population can be recovered when including additional information, as shown in [Fig. 9](#).

We recognise that our joint source fits are conceptually similar to the “stacking” technique that has been used in previous point source searches to increase sensitivity to particular source modelling assumptions (e.g. [Glauch et al. 2023](#)). Case 1) is most similar to a distance-weighted stacking analysis and case 3) is similar to a flux-weighted stacking analysis. However, an important difference is that the priors and modelling that we use are set up in a way such that relevant uncertainties are included and the data can overrule the prior

in more informative cases. This modelling, together with the interpretation offered by the Bayesian approach results in a more flexible analysis.

Cases 1) and 2) explore the possibility that all sources are the same (“complete pooling”) and that all sources are independent (“no pooling”), respectively. Neither of these assumptions are completely realistic, and in practice we expect some balance between global and individual source properties (“partial pooling”), as modelled in our simulation. We see for case 2) that the neutrino data alone does not contain enough information to significantly constrain the population hyperparameters (the shape of the luminosity function and spectral index distribution). However, the future increase in performance expected from planned experiments mentioned in [Section 1](#) will provide the data sets necessary for the “partial pooling” case to be leveraged, and we plan to explore the impact of these new possibilities in upcoming work.

Thanks to the implementation of our statistical model with [Stan’s](#) Hamiltonian Monte Carlo algorithm, we are able to perform fits with over ~ 7000 free parameters in [Section 3.3](#), where the majority of the free parameters are the latent E of the events. In principle, these latent E parameters could be marginalised over in the likelihood to speed up the fits, but as discussed in [Section 2.3](#) and demonstrated in [Section 3.2](#), these parameters add to the interpretability of the results. By including these free parameters here, we also demonstrate that it is relatively straightforward to add further model complexity in terms of parameters for both the source modelling and detector modelling. Large numbers of free parameters can be challenging for optimisers currently implemented in [SkyLLH](#), as it was not designed to fit the latent E parameters or more complex source models. Markov chain Monte Carlo methods, such as those used here, could also be implemented in a frequentist setting to address these challenges.

Another way in which we include more complexity in this work is that we model the atmospheric and diffuse background components, while keeping the total number of expected events conserved. In this way, if events are fit to point sources, the diffuse astrophysical and/or atmospheric components are reduced to

compensate. This approach is interesting when considering the bigger picture of possible neutrino sources, with competing source populations expected (e.g., [Bartos et al. 2021](#)), in addition to contributions from the Galactic plane.

A challenge of the frequentist hypothesis testing approach arises when testing multiple hypotheses, necessitating a trial correction factor. Consequently, source lists for studies have to be limited or the discovery threshold raised, leading to less use of the data and decreased sensitivity. Furthermore, it is non-trivial to keep track of trial factors across independent analyses of the same data. While the Bayesian methods used here do not guarantee a certain false positive rate, the structure included through the priors and hierarchy of our model naturally tends to mitigate the effects of outliers ([Gelman et al. 2009](#)). Should a certain false positive rate be desired, it is possible to calibrate the probability thresholds introduced in [Section 2.3](#) through repeated simulation and fits, as detailed in [Betancourt \(2018\)](#).

Along with guaranteed coverage and false positive rates, one complementary aspect of the standard approach is that by focusing on rejecting background, unexpected signals can be identified even if the alternate hypothesis is not well-specified. In our approach, mismodelling can also be studied with PPCs and used to improve models for a better match with the data. Additionally, computational challenges mean that our approach is currently better suited to building and testing specific point source models rather than performing an uninformed scan across the whole sky. Our implementation in `Stan` includes within-chain parallelisation of the likelihood evaluation that can be scaled according to the available computational resources. As a benchmark, for point sources near the Equator where event rates are the largest, fits using 10 years of data selected in an ROI of 5° radius may take up to 2 hours on 144 threads.

5. CONCLUSIONS

We present a hierarchical Bayesian approach to searching for point sources of astrophysical neutrinos. Our method is an alternative to existing frequentist approaches, with a focus on the characterisation of sources and interpretability of results.

We demonstrate our approach through application to a simulated data set containing 6 weak point sources hidden in typical backgrounds. Even for low event numbers of $n_j \leq 14$, we are able to recover the contribution of the strongest source and provide constraints on its luminosity and spectral index. The contribution of the remaining sources can also be inferred by leveraging similar source properties and more informative priors for their spectral shape. These results show the potential gain of more complex and flexible modelling when studying weak sources that is relevant to the expected signals from current neutrino source candidates, such as blazars or Seyfert galaxies.

We plan to apply our framework to the existing public data sets, investigate the impact of more complex source modelling, and study the information gain from expected future data sets. Our framework is written in a modular way, such that it can also be extended to other event types and detectors, providing a useful open-source tool to the community for the evaluation of different astrophysical models and detector configurations.

ACKNOWLEDGMENTS

The authors express their thanks to Chiara Bellenghi and Martin Wolf for very helpful discussions about the used data set, Lena Saurenhaus for contributing to the production of [Fig. 3](#). The authors are also grateful to Allen Caldwell and Daniel Mortlock for feedback on an early version of this manuscript.

Julian Kuhlmann acknowledges support from the DFG through the Sonderforschungsbereich SFB 1258 “Neutrinos and Dark Matter in Astro- and Particle Physics” (NDM). Francesca Capel acknowledges the financial support from the Excellence Cluster ORIGINS, which is funded by the Deutsche Forschungsgemeinschaft (DFG, German Research Foundation) under Germany’s Excellence Strategy - EXC-2094-390783311 at the early stage of this work.

Facilities: Computations were performed on the HPC system Raven at the Max Planck Computing and Data Facility.

Software: `stan` and `cmdstanpy` ([Stan Development Team 2024](#)), `astropy` ([Astropy Collaboration et al. 2013, 2018](#)), `numpy` ([Harris et al.](#)

2020), `matplotlib` (Hunter 2007), `scipy` (Virtanen et al. 2020), `h5py` (Collette 2013; Collette et al. 2023), `arviz` (Kumar et al. 2019)

APPENDIX

A. DETECTOR MODEL

Using the information provided in the publicly available IRFs (IceCube Collaboration 2021), we can calculate the number of expected events in a sample as

$$\bar{n}_\nu^{\text{tot}} = T \int_{E_{\text{min}}}^{E_{\text{max}}} dE \int_{\hat{E}_{\text{min}}}^{\hat{E}_{\text{max}}} d\hat{E} \int_{S_2} d\omega \int_{\text{ROI}} d\hat{\omega} \frac{d^4 n}{dE dt dA d\omega} A_{\text{eff}}(E, \omega) \text{IRF}(\hat{E}|E, \omega) \text{IRF}(\hat{\omega}|\omega, E, \hat{E}), \quad (\text{A1})$$

where T is the total observation time, ROI is the region of interest and S_2 the surface of a sphere. The integrals over solid angle reflect the modelling of the sources and the cuts on reconstructed direction, respectively. In fits, the angular resolution is modelled using a Rayleigh distribution embedded on a sphere, for a derivation see Glauch (2021). In simulations, $\sigma_{\hat{\omega}}$ is sampled from the provided IRFs.

Due to the required differentiability of the model likelihood with respect to the neutrino energy, we have to interpolate the provided energy resolution, which is provided as histograms in reconstructed energies, covering half a decade of neutrino energy, split over three declination bands. For each histogram $\text{Pr}(\hat{E}|E)$ we fill zero-entries in between non-zero entries by interpolation and extend the empty flanks by a steep power-law with index ± 15 . After renormalising to unity, we stack the histograms' logarithm along a new axis of logarithmic neutrino energy and create a two-dimensional spline representation. Evaluations of this spline at each \hat{E} over a dense grid of $\log_{10}(E)$ is handed over to `Stan` for interpolation. Similarly, we interpolate the logarithm of effective area over logarithmic energies.

As the provided instrument response is only valid for events originating as neutrinos we are restricted to analysis in the Northern hemisphere, as in the Southern hemisphere the event rate is dominated by atmospheric muons.

B. EVENT-SOURCE ASSOCIATION

We can construct an association probability of events to source components by ratios of rate parameters. For every event, we define a categorical variable λ_i , taking on possible values $1, \dots, N_c$:

$$\text{Pr}(\lambda_i = j | \hat{E}, \hat{\omega}, \Theta) = \frac{r_j(\hat{E}, \hat{\omega} | \Theta_j)}{\sum_{l=1}^{N_c} r_l(\hat{E}, \hat{\omega} | \Theta_l)}, \quad (\text{B2})$$

This expression evaluated for the point source and marginalised over the joint posterior is used as colour scale in Fig. 6. We refer for more details to Streit (2010, Chapter 3.2) and the `Stan` documentation⁴.

REFERENCES

- Aartsen, The IceCube Collaboration, Fermi-LAT, et al. 2018a, *Science*, 361, eaat1378, doi: [10.1126/science.aat1378](https://doi.org/10.1126/science.aat1378)
- Aartsen, M., Ackermann, M., Adams, J., et al. 2018b, *Science*, 825, eaat2890, doi: [10.1126/science.aat2890](https://doi.org/10.1126/science.aat2890)
- . 2020a, *Physical Review Letters*, 124, doi: [10.1103/physrevlett.124.051103](https://doi.org/10.1103/physrevlett.124.051103)
- Aartsen, M. G., Ackermann, M., Adams, J., et al. 2017, *Journal of Instrumentation*, 12, P03012, doi: [10.1088/1748-0221/12/03/p03012](https://doi.org/10.1088/1748-0221/12/03/p03012)
- ⁴ <https://mc-stan.org/docs/stan-users-guide/finite-mixtures.html#recovering-posterior-mixture-proportions>

- . 2020b, *Physical Review Letters*, 124, 051103, doi: [10.1103/physrevlett.124.051103](https://doi.org/10.1103/physrevlett.124.051103)
- Aartsen, M. G., Abbasi, R., Ackermann, M., et al. 2021, *Journal of Physics G: Nuclear and Particle Physics*, 48, 060501, doi: [10.1088/1361-6471/abbd48](https://doi.org/10.1088/1361-6471/abbd48)
- Abbasi, R., Ackermann, M., Adams, J., et al. 2022a, *Science*, 378, 538, doi: [10.1126/science.abg3395](https://doi.org/10.1126/science.abg3395)
- . 2022b, *The Astrophysical Journal*, 928, 50, doi: [10.3847/1538-4357/ac4d29](https://doi.org/10.3847/1538-4357/ac4d29)
- . 2023, *Science*, 380, 1338, doi: [10.1126/science.adc9818](https://doi.org/10.1126/science.adc9818)
- . 2024, Characterization of the Astrophysical Diffuse Neutrino Flux using Starting Track Events in IceCube. <https://arxiv.org/abs/2402.18026>
- Adrián-Martínez, S., Ageron, M., Aharonian, F., et al. 2016, *Journal of Physics G: Nuclear and Particle Physics*, 43, 084001, doi: [10.1088/0954-3899/43/8/084001](https://doi.org/10.1088/0954-3899/43/8/084001)
- Ageron, M., Aguilar, J. A., Samarai, I. A., et al. 2011, *Nuclear Instruments and Methods in Physics Research Section A: Accelerators, Spectrometers, Detectors and Associated Equipment*, 656, 11, doi: [10.1016/j.nima.2011.06.103](https://doi.org/10.1016/j.nima.2011.06.103)
- Aggarwal, K., Budavári, T., Deller, A. T., et al. 2021, *The Astrophysical Journal*, 911, 95, doi: [10.3847/1538-4357/abe8d2](https://doi.org/10.3847/1538-4357/abe8d2)
- Agostini, M., Böhmer, M., Bosma, J., et al. 2020, *Nature Astronomy*, 4, 913, doi: [10.1038/s41550-020-1182-4](https://doi.org/10.1038/s41550-020-1182-4)
- Ashton, G., Burns, E., Canton, T. D., et al. 2018, *The Astrophysical Journal*, 860, 6, doi: [10.3847/1538-4357/aabfd2](https://doi.org/10.3847/1538-4357/aabfd2)
- Astropy Collaboration, Robitaille, T. P., Tollerud, E. J., et al. 2013, *A&A*, 558, A33, doi: [10.1051/0004-6361/201322068](https://doi.org/10.1051/0004-6361/201322068)
- Astropy Collaboration, Price-Whelan, A. M., Sipócz, B. M., et al. 2018, *AJ*, 156, 123, doi: [10.3847/1538-3881/aabc4f](https://doi.org/10.3847/1538-3881/aabc4f)
- Avrorin, A. D., Avrorin, A. V., Aynutdinov, V. M., et al. 2021, *Physics of Atomic Nuclei*, 84, 513, doi: [10.1134/s1063778821040062](https://doi.org/10.1134/s1063778821040062)
- Bartos, I., Veske, D., Keivani, A., et al. 2019, *Physical Review D*, 100, 083017, doi: [10.1103/physrevd.100.083017](https://doi.org/10.1103/physrevd.100.083017)
- Bartos, I., Veske, D., Kowalski, M., Márka, Z., & Márka, S. 2021, *The Astrophysical Journal*, 921, 45, doi: [10.3847/1538-4357/ac1c7b](https://doi.org/10.3847/1538-4357/ac1c7b)
- Bellenghi, C., Karl, M., Wolf, M., et al. 2023a, in *Proceedings of 38th International Cosmic Ray Conference — PoS(ICRC2023)*, Vol. 444, 1061, doi: [10.22323/1.444.1061](https://doi.org/10.22323/1.444.1061)
- Bellenghi, C., Padovani, P., Resconi, E., & Giommi, P. 2023b, *The Astrophysical Journal Letters*, 955, L32, doi: [10.3847/2041-8213/acf711](https://doi.org/10.3847/2041-8213/acf711)
- Belolaptikov, I., Bezrukov, L., Borisovets, B., et al. 1997, *Astroparticle Physics*, 7, 263, doi: [10.1016/s0927-6505\(97\)00022-4](https://doi.org/10.1016/s0927-6505(97)00022-4)
- Betancourt, M. 2018, *Calibrating Model-Based Inferences and Decisions*. <https://arxiv.org/abs/1803.08393>
- Braun, J., Baker, M., Dumm, J., et al. 2010, *Astroparticle Physics*, 33, 175, doi: [10.1016/j.astropartphys.2010.01.005](https://doi.org/10.1016/j.astropartphys.2010.01.005)
- Braun, J., Dumm, J., Palma, F. D., et al. 2008, *Astroparticle Physics*, 299, doi: [10.1016/j.astropartphys.2008.02.007](https://doi.org/10.1016/j.astropartphys.2008.02.007)
- Budavári, T., & Loredó, T. J. 2015, *Annual Review of Statistics and Its Application*, 2, 113, doi: [10.1146/annurev-statistics-010814-020231](https://doi.org/10.1146/annurev-statistics-010814-020231)
- Burgess, J., & Capel, F. 2021, *Journal of Open Source Software*, 6, 3257, doi: [10.21105/joss.03257](https://doi.org/10.21105/joss.03257)
- Buson, S., Tramacere, A., Pfeiffer, L., et al. 2022, *The Astrophysical Journal Letters*, 933, L43, doi: [10.3847/2041-8213/ac7d5b](https://doi.org/10.3847/2041-8213/ac7d5b)
- Buson, S., Tramacere, A., Oswald, L., et al. 2023, *Extragalactic neutrino factories*. <https://arxiv.org/abs/2305.11263>
- Capel, F., Kuhlmann, J., Haack, C., et al. 2023, in *ICRC 2023, Proceedings of 38th International Cosmic Ray Conference — PoS(ICRC2023)*, 1576, doi: [10.22323/1.444.1576](https://doi.org/10.22323/1.444.1576)
- Capel, F., & Mortlock, D. J. 2019, *Monthly Notices of the Royal Astronomical Society*, 484, 2324–2340, doi: [10.1093/mnras/stz081](https://doi.org/10.1093/mnras/stz081)
- Capel, F., Mortlock, D. J., & Finley, C. 2020, *Physical Review D*, 101, 123017, doi: [10.1103/physrevd.101.123017](https://doi.org/10.1103/physrevd.101.123017)
- Collette, A. 2013, *Python and HDF5* (O'Reilly)
- Collette, A., Kluyver, T., Caswell, T. A., et al. 2023, *h5py/h5py: 3.8.0, 3.8.0*, Zenodo, doi: [10.5281/zenodo.7560547](https://doi.org/10.5281/zenodo.7560547)
- Dvornicky, R. 2023, in *Proceedings of 38th International Cosmic Ray Conference — PoS(ICRC2023)*, Vol. 444, 976, doi: [10.22323/1.444.0976](https://doi.org/10.22323/1.444.0976)

- Fedynitch, A., Engel, R., Gaisser, T. K., Riehn, F., & Stanev, T. 2015, Calculation of conventional and prompt lepton fluxes at very high energy. <https://arxiv.org/abs/1503.00544>
- Gaisser, T. K. 2012, *Astroparticle Physics*, 35, 801, doi: [10.1016/j.astropartphys.2012.02.010](https://doi.org/10.1016/j.astropartphys.2012.02.010)
- Gelman, A., Carlin, J. B., Stern, H. S., et al. 2013, *Bayesian Data Analysis*, 3rd edn. (Chapman and Hall/CRC), doi: [10.1201/b16018](https://doi.org/10.1201/b16018)
- Gelman, A., Hill, J., & Yajima, M. 2009, Why we (usually) don't have to worry about multiple comparisons. <https://arxiv.org/abs/0907.2478>
- Giommi, P., & Padovani, P. 2021, *Universe*, 7, 492, doi: [10.3390/universe7120492](https://doi.org/10.3390/universe7120492)
- Glauch, T. 2021, PhD thesis, Technische Universität München
- Glauch, T., Kheirandish, A., Kontrimas, T., et al. 2023, in *Proceedings of 38th International Cosmic Ray Conference — PoS(ICRC2023)*, Vol. 444, 1052, doi: [10.22323/1.444.1052](https://doi.org/10.22323/1.444.1052)
- Harris, C. R., Millman, K. J., van der Walt, S. J., et al. 2020, *Nature*, 585, 357, doi: [10.1038/s41586-020-2649-2](https://doi.org/10.1038/s41586-020-2649-2)
- Hunter, J. D. 2007, *Computing in Science & Engineering*, 9, 90, doi: [10.1109/MCSE.2007.55](https://doi.org/10.1109/MCSE.2007.55)
- IceCube Collaboration. 2021, *IceCube Data for Neutrino Point-Source Searches Years 2008-2018*, IceCube Neutrino Observatory, doi: [10.21234/CPKQ-K003](https://doi.org/10.21234/CPKQ-K003)
- Kowalski, M. 2021, *Nature Astronomy*, 5, 732, doi: [10.1038/s41550-021-01431-y](https://doi.org/10.1038/s41550-021-01431-y)
- Kumar, R., Carroll, C., Hartikainen, A., & Osvaldo, M. 2019, *Journal of Open Source Software*, doi: [10.21105/joss.01143](https://doi.org/10.21105/joss.01143)
- Kurahashi, N., Murase, K., & Santander, M. 2022, *Annual Review of Nuclear and Particle Science*, 72, 365
- Madau, P., & Dickinson, M. 2014, *Annu. Rev. Astron. Astrophys.*, 52, 415, doi: [10.1146/annurev-astro-081811-125615](https://doi.org/10.1146/annurev-astro-081811-125615)
- Margiotta, A. 2022, *The KM3NeT infrastructure: status and first results*. <https://arxiv.org/abs/2208.07370>
- Murase, K., & Waxman, E. 2016, *Physical Review D*, D94, 103006, doi: [10.1103/physrevd.94.103006](https://doi.org/10.1103/physrevd.94.103006)
- Naab, R., et al. 2023, in *Proceedings of 38th International Cosmic Ray Conference — PoS(ICRC2023)*, Vol. 444, 1064, doi: [10.22323/1.444.1064](https://doi.org/10.22323/1.444.1064)
- Neronov, A., Savchenko, D., & Semikoz, D. V. 2024, *Physical Review Letters*, 132, 101002, doi: [10.1103/physrevlett.132.101002](https://doi.org/10.1103/physrevlett.132.101002)
- Neronov, A., Semikoz, D., & Savchenko, D. 2023, Neutrino signal from Cygnus region of the Milky Way. <https://arxiv.org/abs/2311.13711>
- Picone, J. M., Hedin, A. E., Drob, D. P., & Aikin, A. C. 2002, *Journal of Geophysical Research: Space Physics*, 107, SIA 15, doi: [10.1029/2002ja009430](https://doi.org/10.1029/2002ja009430)
- Reusch, S., Stein, R., Kowalski, M., et al. 2022, *Physical Review Letters*, 128, 221101, doi: [10.1103/physrevlett.128.221101](https://doi.org/10.1103/physrevlett.128.221101)
- Riehn, F., Dembinski, H., Engel, R., et al. 2017, in *ICRC 2017, Proceedings of 35th International Cosmic Ray Conference — PoS(ICRC2017)*, 301, doi: [10.22323/1.301.0301](https://doi.org/10.22323/1.301.0301)
- Saurenhaus, L., & Capel, F. 2023, in *Proceedings of 38th International Cosmic Ray Conference — PoS(ICRC2023)*, Vol. 444, 1509, doi: [10.22323/1.444.1509](https://doi.org/10.22323/1.444.1509)
- Sottosanti, A., Bernardi, M., Brazzale, A. R., et al. 2021, Identification of high-energy astrophysical point sources via hierarchical Bayesian nonparametric clustering. <https://arxiv.org/abs/2104.11492>
- Stan Development Team. 2024, *Stan Modeling Language Users Guide and Reference Manual*. <http://mc-stan.org/>
- Stein, R., Velzen, S. v., Kowalski, M., et al. 2021, *Nature Astronomy*, 1, doi: [10.1038/s41550-020-01295-8](https://doi.org/10.1038/s41550-020-01295-8)
- Streit, R. L. 2010, *Poisson Point Processes: Imaging, Tracking, and Sensing*, 1st edn. (Springer New York, NY), doi: [10.1007/978-1-4419-6923-1](https://doi.org/10.1007/978-1-4419-6923-1)
- van Velzen, S., Stein, R., Gilfanov, M., et al. 2021, Establishing accretion flares from massive black holes as a major source of high-energy neutrinos. <https://arxiv.org/abs/2111.09391>
- Veske, D., Márka, Z., Bartos, I., & Márka, S. 2021, *The Astrophysical Journal*, 908, 216, doi: [10.3847/1538-4357/abd542](https://doi.org/10.3847/1538-4357/abd542)
- Virtanen, P., Gommers, R., Oliphant, T. E., et al. 2020, *Nature Methods*, 17, 261, doi: [10.1038/s41592-019-0686-2](https://doi.org/10.1038/s41592-019-0686-2)
- Wolf, M. 2019, in *Proceedings of 36th International Cosmic Ray Conference — PoS(ICRC2019)*, Vol. 358, 1035, doi: [10.22323/1.358.1035](https://doi.org/10.22323/1.358.1035)

Ye, Z. P., Hu, F., Tian, W., et al. 2023, *Nature Astronomy*, 7, 1497,
doi: [10.1038/s41550-023-02087-6](https://doi.org/10.1038/s41550-023-02087-6)